Anhydrous Phase B: Transmission Electron Microscope Characterization and Elastic Properties

A. Addad[1], P. Carrez[1], P. Cordier[1] iD, D. Jacob[1] iD, S.-I. Karato[2] iD, A. Mohiuddin[2] iD, A. Mussi[1] iD, B. C. Nzogang[1], P. Roussel[3] iD, and A. Tommasi[4] iD

[1]Université de Lille, CNRS, INRA, ENSCL, UMR 8207 - UMET - Unité Matériaux et Transformations, Lille, France, [2]Department of Geology and Geophysics, Yale University, New Haven, CT, USA, [3]Université de Lille, CNRS, Centrale Lille, ENSCL, Université d'Artois, UMR 8181 - UCCS - Unité de Catalyse et de Chimie du Solide, Lille, France, [4]Université de Montpellier, CNRS, Geosciences Montpellier, Montpellier, France

Abstract We have performed an extensive characterization by transmission electron microscopy (including precession electron diffraction tomography and ab initio electron diffraction refinement as well as electron energy loss spectroscopy) of anhydrous phase B (Anh-B) formed directly from olivine at 14 GPa, 1400 °C. We show that Anh-B, which can be considered as a superstructure of olivine, exhibits strong topotactic relationships with it. This lowers the interfacial energy between the two phases and the energy barrier for nucleation of Anh-B, which can form as a metastable phase. We have calculated the elastic and seismic properties of Anh-B. From the elastic point of view, Anh-B appears to be more isotropic than olivine. Anh-B displays only a moderate seismic anisotropy quite similar to the one of wadsleyite.

Plain Language Summary Anhydrous phase B (Anh-B) is a dense magnesium silicate with composition $(Mg, Fe)_{14}Si_5O_{24}$, which is expected to form in Mg-rich or Si-depleted regions of the mantle. We show that due to strong crystallographic similarities with the crystal structure of olivine, it can form directly from it as a metastable phase. We show that Anh-B exhibits a moderate seismic anisotropy, which makes its detection difficult in the mantle.

1. Introduction

The sequence of phase transformations of the major rock-forming minerals with increasing temperature and pressure in the Earth's mantle is relatively well understood. The most abundant mineral in the upper mantle, olivine, transforms to wadsleyite at 410 km (approximately 14 GPa; Katsura et al., 2004), which then transforms to ringwoodite at 520 km (≈18 GPa near 1600 K; Katsura & Ito, 1989; Akaogi et al., 1989). The second most abundant mineral, orthopyroxene, undergoes gradual transformation (completed in the pressure interval 14-16 GPa) to majorite garnet through the reaction with pyrope garnet (e.g., Irifune, 1987; Ringwood, 1991). Then ringwoodite and majorite react to form a mixture of bridgmanite and ferropericlase (at approximately 23-24 GPa; Hirose, 2002). Through these phase transformations, the minerals change to denser crystal structures. These changes are sometimes associated with a change in the coordination of oxygen ions surrounding a cation, in particular silicon (Finger & Hazen, 1991).

In these two-phase transformation sequences, the (Mg+Fe)/Si ratio is between 1 and 2 (1 for orthopyroxene and 2 for olivine). Although these two sequences explain a majority of seismological observations, the role of some minor phases is often invoked to explain some geological observations. An important case is the anhydrous phase B (Anh-B), which has an unusually high (Mg+Fe)/Si ratio (2.8; Finger et al., 1991). For example, Ganguly and Frost (2006) investigated the stability of Anh-B and suggested that it be an explanation of the so-called X discontinuity that has been reported at 275- to 345-km depth in several subcontinental and subduction zone environments. Yuan et al. (2018) extended such a study to higher pressures and proposed that Anh-B could offer an alternative interpretation of the origin of the paragenesis of olivine and periclase found in some natural diamonds.

However, in both studies, the stability of Anh-B phase relative to olivine (or wadsleyite or ringwoodite) + MgO was studied in a system with a very high Mg/Si ratio (=2.8). In the real Earth, (Mg+Fe)/Si is lower (=1-2) and a more likely reaction is the formation of Anh-B and stishovite from olivine

(or wadsleyite or ringwoodite). However, the details of this reaction remain unclear. Ganguly and Frost (2006) calculated the thermodynamic parameters of Anh-B and predicted that Anh-B + stishovite might be present in a cold slab. However, this prediction has not been tested experimentally.

In this study, we report an extensive characterization by transmission electron microscopy (TEM) of lamellae of Anh-B formed in a sample of polycrystalline olivine annealed at 14 GPa, 1400 °C. Structure refinement is performed from processing three-dimensional precession electron diffraction data. The structure model is complemented by chemical analysis by energy-dispersive X-ray spectroscopy (EDS), and silicon coordination is characterized by electron energy loss spectroscopy (EELS) analyses. From this structure model, first-principles atomic scale calculations are carried out to investigate the stability of this phase and to determine its elastic properties, and then its seismic properties.

2. Experiments and Microstructural Characterization

2.1. High-Pressure Synthesis

Large single crystals of San Carlos olivine with no visible inclusions were handpicked and crushed to make a fine-grained powder by cold pressing in a hydraulic press. The powder was then sorted to obtain ~5- to 10-μm grains by suspension method. The powder was then cold pressed in a hydraulic press and then vacuum sintered in a furnace oven at 1200 °C for 12 hr to obtain a dense polycrystalline aggregate of San Carlos olivine. The dense olivine aggregate was then core drilled to obtain a cylindrical sample of 1.8-mm length and 1.8-mm diameter.

High-pressure and high-temperature experiments were carried out in a KIWI 1000-ton Kawai-type multianvil apparatus installed at Yale University. A 10-mm edge length Cr_2O_3-doped MgO octahedron with 5-mm truncation edge length of WC anvils was used for pressure generation. A 40-μm-thick rhenium foil was used as a heater, which was inserted in a ZrO_2 thermal insulation sleeve for heating. A W_5Re-$W_{26}Re$ thermocouple was used to monitor the temperature. All the ceramic parts were fired at 1000 °C for 12 hr to remove adsorbed water prior to high-pressure experiments.

The pressure was calibrated as function of hydraulic oil pressure using the experimental results on the olivine-wadsleyite transformation (P = 14 GPa at T = 1400 °C) by Katsura et al. (2004). The temperature distribution in the cell assembly was mapped using the enstatite-diopside thermometry at 15 GPa (Gasparik, 1996). Temperature within the sample did not vary by more than ~30 K. In the experiment reported here, pressure was increased to 14 GPa over a period of 5 hr. After reaching the desired pressure, temperature was increased rapidly to 1400 °C (>100 °C per min). The sample was then annealed at 1400 °C for 30 min.

Scanning electron microscopy (SEM) examination of the recovered sample showed that olivine was partially transformed into denser (appearing brighter in backscattered mode) phases with two distinct morphologies. Intragranular or intergranular domains with irregular but often rounded shapes and some thin planar lamellae (Figure 1).

2.2. Microstructural, Structural, and Chemical Investigation by TEM
2.2.1. Sample Preparation
Electron-transparent foils for TEM containing the lamellae were extracted using the focus ion beam (FIB) technique with a FIB Dual Beam FEI Strata DB 235 at IEMN-Lille, France. Figure 1 shows the location in the sample of one of the FIB sections. The thin section was lifted off below the line, perpendicular to the surface.

2.2.2. Microstructural Investigation
TEM observations were carried out using a FEI® Tecnai G2-20 twin microscope operating at 200 kV and a Philips CM30 microscope operating at 300 kV, both equipped with a LaB_6 filament and using a double tilt sample-holder. Automated crystal orientation mapping in TEM (ACOM-TEM) was operated in the TEM with the ASTAR^{TM} tool from NanoMEGAS. As on SEM images, one can observe within and at the limits of olivine crystals irregularly shaped grains, which are indexed with ACOM-TEM as wadsleyite, and a planar lamella located at the boundary between two olivine grains (Figure 2). With ACOM-TEM, the lamella can be indexed neither as olivine nor as wadsleyite.
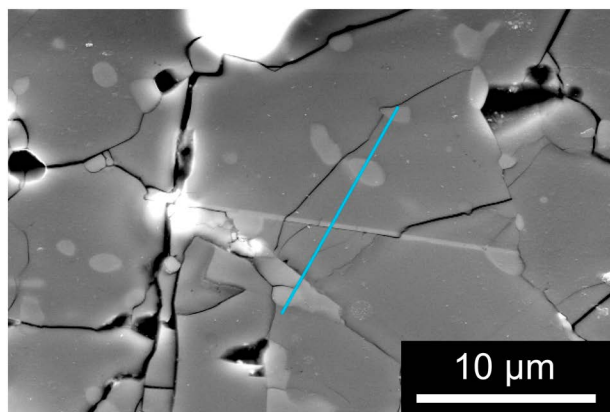
Figure 1. Scanning electron microscopy examination of the run product of experiment K1487 annealed at 14 GPa, 1400 °C for 30 min. Transformation products appear in light gray as either irregular domains or planar lamellae, which are of interest in this study. The blue line shows the location of focus ion beam section, which crosscuts a well-developed lamella.

In diffraction contrast (Figure 3), wadsleyite displays characteristic planar defects in (010). The lamella is free of defects. It exhibits a crystallographic relationship with one of the olivine grains illustrated in Figure 3b where both the lamella and olivine grain 2 show similar contrast in weak-beam dark-field. A network of misfit dislocations is observed at the interface between the two phases (Figure 3b). This lamella located at the boundary between two olivine grains, which was clearly visible in the SEM images, is however not unique. Several thinner lamellae, which cannot be detected at the SEM scale, with the same orientation as the large lamella are observed within the olivine crystals (Figure 3c).

2.2.3. Chemical Analyses by EDS

The chemical composition of the lamella has been determined with an EDS by scanning transmission electron microscopy spectrum image mode in the Thermo Fischer® Titan Themis TEM, operated at 300 kV. Quantification has been carried out on the basis of the stoichiometric oxides of the Van Cappellen and Doukhan (1994) method. The k-factors (Cliff & Lorimer, 1975) have been obtained using stoichiometric oxide standard specimens which contain the studied phase elements.
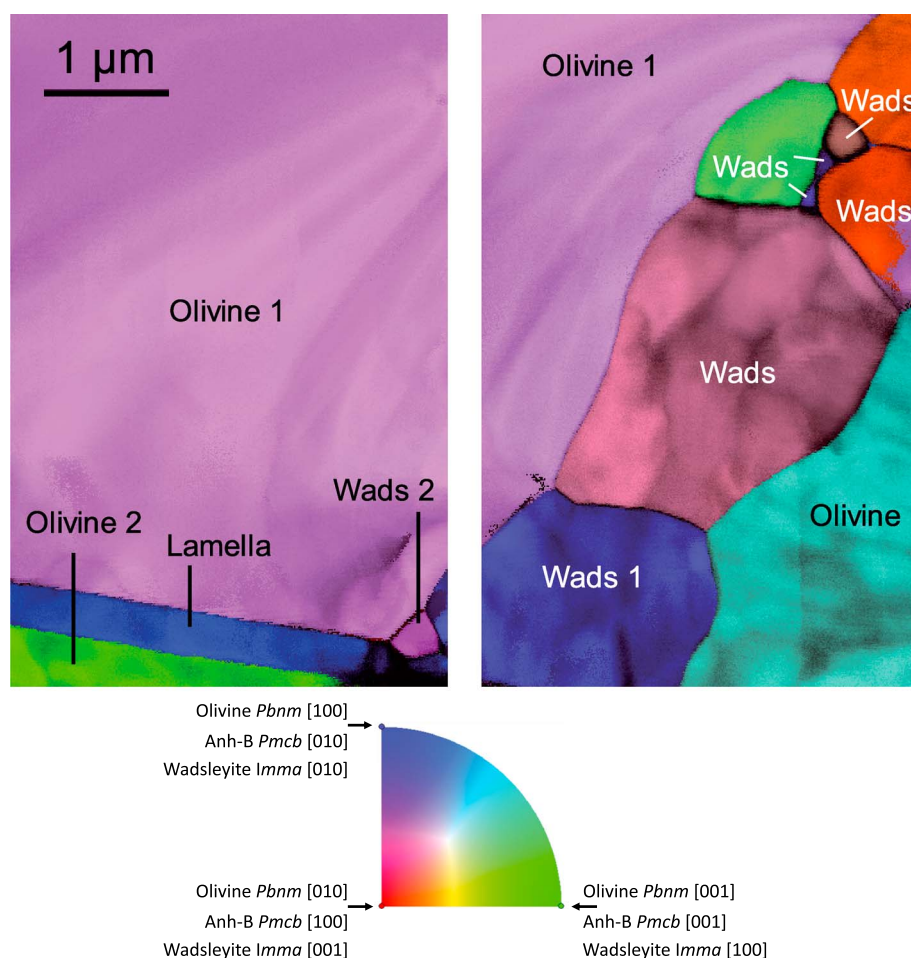

Figure 2. Two adjacent (with a small gap in between) orientation maps from the focus ion beam foil extracted from the location indicated on Figure 1. Spatial resolution: 10 nm. 550 × 350 data points. Precession angle 0.5°. The inverse pole figures represented here correspond to the vertical direction. They are superimposed with the reliability maps. Additional inverse pole figures (corresponding to the vertical and normal-to-plane directions), as well as the phase map, are provided in the supporting information. The color code is provided for the crystal orientations of the three phases.
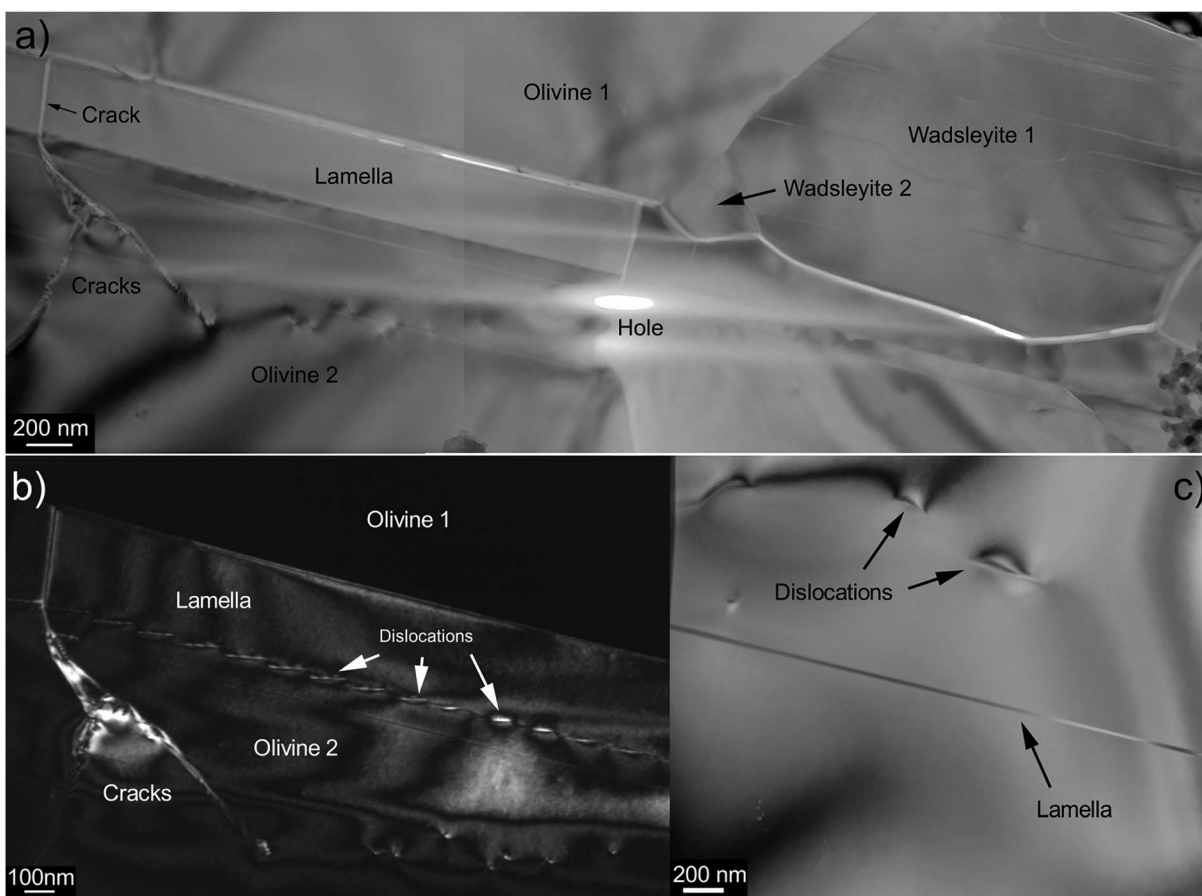
Figure 3. Conventional (diffraction contrast) transmission electron microscopy image of the area containing the lamella in the focus ion beam section, which location of extraction is shown in Figure 1. (a) Bright field image showing the lamella between two olivine grains and next to two wadsleyite grains. This area is mapped at the bottom of Figure 2. The small hole results from the ion thinning process. Several cracks are visible which probably result from decompression and/or specimen thinning. (b) Weak-beam dark-field image ($\mathbf{g}$ = 004 for olivine and $\mathbf{g}$ = 400 for anhydrous phase B) showing that the lamella and the olivine 2 grain are in topotactic relationship and exhibit a network of misfit dislocations at the interface. (c) Bright-field image from the "olivine 2" grain showing one of the thin lamellae observed within this grain.

Chemical maps are shown on Figure 4. Iron and nickel concentrations are higher in the lamella than in olivine, but, more importantly, the lamella shows significant deficiency in silicon compared to olivine. EDS analyses were performed inside and on both sides of the lamella. To ensure the accuracy of the quantifications, we have verified that the phase composition around the lamella matches with stoichiometric olivine and wadsleyite. We have found on both sides of the lamella, compositions of $Mg_{1.75}Fe_{0.2}Ni_{0.05}Si_{0.99}O_{4.01}$ and $Mg_{1.89}Fe_{0.1}Ni_{0.01}SiO_4$ for wadsleyite and olivine, respectively. Both minerals display therefore a general composition of $(Mg, Fe, Ni)_2SiO_4$, with a $(Mg+Fe)/Si$ ratio of 2. The composition of the lamella is $Mg_{1.99}Fe_{0.21}Ni_{0.05}Si_{0.84}O_4$, which can also be written as $(Mg, Fe, Ni)_{13.8}Si_{5.04}O_{24}$. It has therefore a $(Mg+Fe)/Si$ ratio of 2.738. Next to the lamella, an ultrafine layer a few nanometers thick (grey arrow in Figures 4b and 4c) is enriched in silicon and oxygen. Quantification of this ultrafine layer is consistent with a SiO_2 composition.

2.2.4. Precession Electron Tomography in the TEM

Precession electron diffraction tomography was carried out on a FEI® Tecnai G2 20 operated at 200 kV and equipped with a NanoMEGAS Digistar precession device and an ORIUS 832 Gatan charge-coupled device camera with 14-bit dynamic range. The diffraction patterns were obtained using a defocused parallel beam and a selected area aperture of about 250 nm in diameter, smaller than the width of the lamellae. The lamella has been orientated in the microscope in such a way that the goniometer tilt axis is kept perpendicular to the interface plane during the tilt experiments only for the lamella that contributed to the collected diffraction patterns series. The electron diffraction pattern tilt series were collected by varying the tilt angle from -45° to
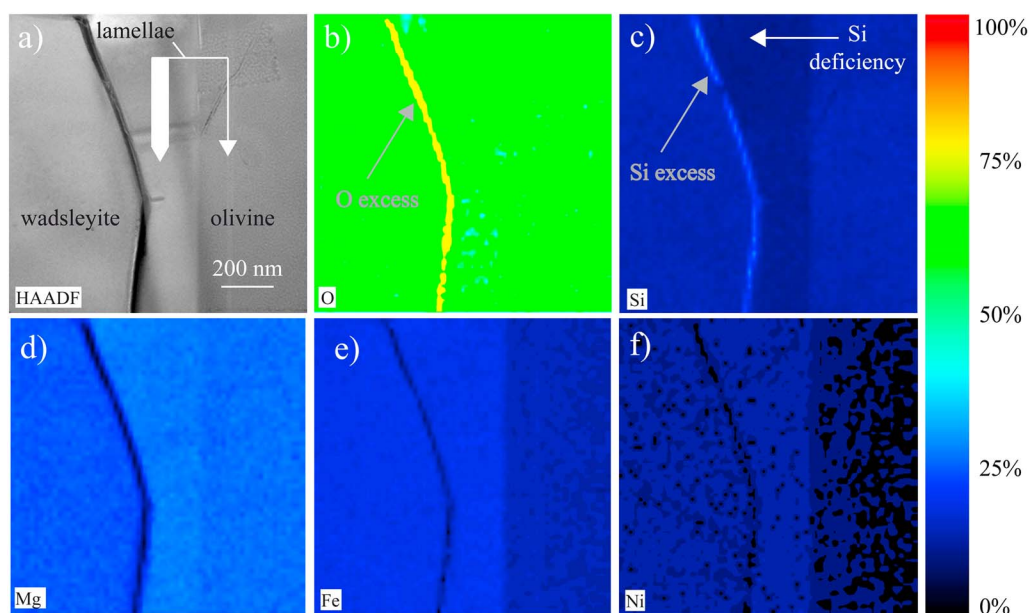
Figure 4. Energy-dispersive X-ray spectroscopy maps of wadsleyite, olivine and the lamellae, located in the same region: (a) High angular annular dark field image of a zone which contains a grain of wadsleyite (on the left), olivine (on the right), and the lamellae (in the middle). Energy-dispersive X-ray spectroscopy scanning transmission electron microscopy spectrum image of (b) oxygen, (c) silicon, (d) magnesium, (e) iron, and (f) nickel. The lamella is deficient in silicon (white arrow in c) relatively to both olivine and wadsleyite and enriched in iron and nickel relatively to olivine. It is rimmed by a silicon- and oxygen-rich thin domain (indicated with a grey arrow in b and c). We can notice another thin lamella inside the olivine grain (thin white arrow in a), which width is below the resolution of the EDS analyzes.

+45° with an acquisition step of 1° (91 patterns for one tilt series). The precession angle was set to 1.2°, slightly higher than the tilt step in order to ensure a full coverage of the reciprocal space within the tilt range. During the tilt series acquisition, the position of the aperture with respect to the lamellae was checked every few degrees.

2.2.5. Crystal Structure Determination and Refinements

Precession electron tomography data processing was performed using the PETS program (Palatinus, 2011). After peak hunting on all patterns, the value of the azimuthal angle (i.e., the angle between the horizontal axis and the projection of the tilt axis) was refined. After clustering, a difference vector space analysis was computed to produce a complete representation of the reciprocal space. The program JANA2006 was then used to find the unit cell ($a = 5.9181(13)$ Å, $b = 10.1141(9)$ Å, $c = 14.3428(13)$ Å, and $V = 858.5(2)$ Å^3) and to refine the orientation matrix, allowing integration of the intensities for each pattern by PETS. At this step, Inorganic Crystal Structure Database as well as American Mineralogist Structure Database were consulted with a 5% tolerance on cell parameters. Since no results were returned, an ab initio structure solution was started. In a first step, a kinematical approach was used and intensities belonging to the same reflection on adjacent patterns were integrated together, leading to a list of intensities containing one value per hkl index with the corresponding estimated standard deviation. The reflection conditions are h0l, l=2n and hk0, k=2n, indicating the possible space group *Pmcb* (number 55, nonstandard setting of *Pbam*).

The structure was then solved ab initio using the charge flipping algorithm, as implemented in the program Superflip (Palatinus & Chapuis, 2007) with the chemical information provided by the EDS analysis ($Mg_{1.99}Fe_{0.21}Si_{0.84}O_4$). After several cycles of calculations, SUPERFLIP found a solution with an overall agreement factor (wR) around 20%, which might be high for X-ray data, but is a rather good value for electron diffraction data considering the remaining dynamical diffraction effects. The [100] projection of the electron density isosurface of the structure solution is presented in Figure 5a, and its interpretation in term of atomic positions (taking into account common tetrahedral or octahedral geometries) is presented in Figure 5b. At this time, considering that (i) tetrahedral sites are occupied by silicon (with Si-O distances between 1.62 and 1.70 A), (ii) "big" octahedral sites (distances between 1.98 and 2.23 A) are occupied by
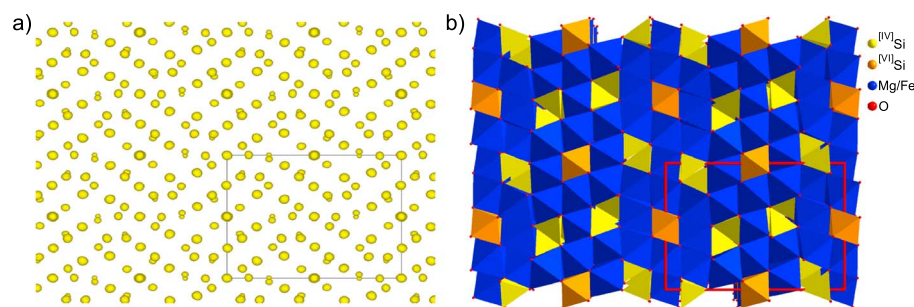
Figure 5. (a) [100] projection of the electron density isosurface of the structure solution. Note that the size of the "balls" is related to the number of electrons on the site, enabling both the identification of the atomic species and the site occupation refinement. (b) [100] projection of the proposed model in term of polyhedral pattern.

magnesium, and (iii) "small" octahedral site (6 distances around 1.81 A) is occupied by iron, an estimated chemical formula would be $Mg_{2.333}Fe_{0.167}Si_{0.667}O_4$.

However, it is now well established that the kinematical approach is not appropriate to determine the correctness of such a build structure (Palatinus, Petříček, & Correa, 2015; Roussel et al., 2014) and that dynamical effects are still present in the data even with beam-precession. The previous model was therefore used as the starting one for dynamical refinement. This still emerging approach has already been used successfully a few times and is now recognized as a good alternative for accurate structure determination and refinement of submicronic samples (Colmont et al., 2016; Palatinus et al., 2017; Rondeau et al., 2019). After several cycles of refinements of both atomic parameters (positions, and thermal ones) and orientation-thickness of the sample, encouraging agreement factors were obtained, supporting the opportunity to go further with this dataset. At this point, several possibilities were tested, such as the possibility to have mixed occupancy of Mg and Fe on big sites and only iron on small ones. This hypothesis leads to better agreement factors and to a chemical formula closest to the EDS-determined one. However, the atomic displacement parameter of the small site (fully occupied by iron in this case) is abnormally high, indicating that this site "possesses too many electrons". A way to decrease the number of electrons assigned on this site is to replace, partly or entirely, the iron ($Z=26$) by silicon ($Z=14$). The two hypotheses were tested, and both lead to close agreement factors (wR around 0.075) and this time reasonable thermal parameters. The refined chemical formulae are $Mg_{1.943}Fe_{0.414}Si_{0.809}O_4$ for a site occupied by 85% of Si and 15% of Fe and $Mg_{1.958}Fe_{0.375}Si_{0.833}O_4$ for a site occupied only by silicon, both very close the EDS one ($Mg_{1.99}Fe_{0.21}Si_{0.84}O_4$). In summary, whatever the chosen model, it is clear that this octahedral site is mostly occupied by silicon.

The dynamical refinement of the precession electron diffraction tomography data yields the structure presented in Figure 5, corresponding in fact to the already known anhydrous phase B (Anh-B; Finger et al., 1989) but described with the alternative setting: a=0.59181(13) nm, b=1.43428(13) nm, and c=1.01141(9) nm. A matrix transformation allows to be in the same setting as Finger et al. (1989), which, for consistency with previously published studies, is used throughout the present paper. The final crystallographic data and refinement details are provided in Table S1 in the supporting information. Fractional coordinates and equivalent isotropic displacement parameters are given in Table S2, while selected interatomic distances are given in Table S3.

2.2.6. EELS Analyses

In silicates, silicon is usually in tetrahedral sites (as in quartz, olivine, or wadsleyite, for instance), but with increasing pressure it can occupy octahedral sites (as in high-pressure phases like stishovite or bridgmanite). To confirm the silicon coordination predicted by the structure refinement, we have characterized its oxygen environments. We have performed EELS analyses and more specifically energy loss near edge structure (ELNES) characterizations. Three ELNES spectra can be used to distinguish between tetrahedral and octahedral sites for silicon: the Si K-edge, Si L2,3-edge, and O K-edge. We have focused our attention on the O K-edge ELNES spectra. Actually, this edge has low core loss energy (near 530 eV) and offers noticeable changes in ELNES signatures from SiO_4 to SiO_6 (Sharp et al., 1996).

EELS analyses have been performed with a Thermo Fischer® Titan Themis TEM, operating at 80 kV to reduce electron beam damage. ELNES structures are analyzed with a monochromated STEM spectrum
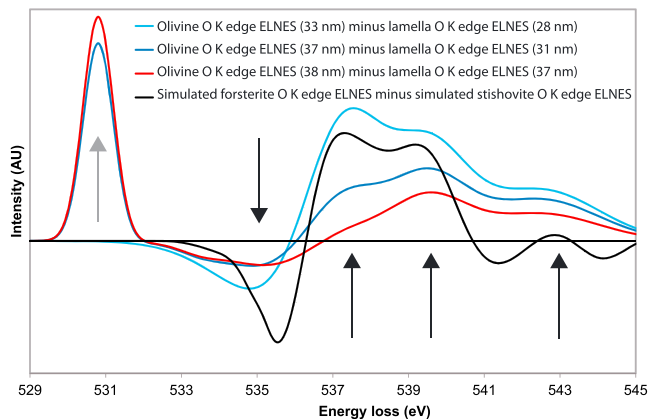
Figure 6. Experimental and simulated differential O K-edge energy loss near edge structure (ELNES) spectra: Specimen degradation noted by a peak appearance of O_2 cluster development (grey arrow at 530.8 eV). The signature of the differential spectra is composed of four peaks (black arrows near 535, 537.5, 539.5, and 543 eV) whose intensities depend on the thickness analyzed zones.

image mode, with an energy resolution of approximately 0.3 eV. In order to detect the ELNES details, the spectrometer energy dispersion was chosen to be 0.025 eV/channel.

To highlight the differences between olivine ELNES structures (where silicon atoms are all in tetrahedral sites) and the ELNES structures of the phase in the lamella (where we suppose the occurrence of silicon atoms in octahedral sites), we have analyzed the "olivine//lamella" differential EELS spectra. The estimated thicknesses indicated in parenthesis on Figure 6 have been obtained by comparing energy-filtered intensities to keep only the elastic electrons, with raw intensities, thanks to the following equation extracted from the Poisson law:

$$I_0/I = \exp(-t/\lambda) \tag{1}$$

where I_0 is the signal intensity obtained with elastic electrons, I is the raw signal intensity, λ is the mean free path, and t is the specimen thickness. From Tanuma et al. (1993), a mean free path of 84 nm has been estimated for olivine with a voltage of 80 kV.

It is worth mentioning a peak appearance at 530.8 eV, already noticed by Mkhoyan et al. (2006) and Garvie (2010) at approximately 531 and 530 eV, respectively. This peak growth has been interpreted as a structure damage leading to O_2 cluster developments. The intensity normalization of differential ELNES spectra is done on the highest peak after the peak observed at 530.8 eV, that is, for an energy starting from 532 eV. Figure 6 shows the normalized differential O K-edge ELNES spectra of olivine//lamella for different zones characterized by different thicknesses since this parameter has a strong influence on the spectra. Whatever the thickness, the lamella is less affected by O_2 cluster developments than olivine, suggesting that the Si─O bonds within the lamella are stronger than in olivine. It can be noticed that there is no peak at 530.8 eV for the smallest thicknesses ($\approx$30 nm), suggesting the impossibility to store O_2 clusters in such thin zones. To compare these experimental results with literature, the simulated O K-edge ELNES spectrum of forsterite (the pure magnesia pole of olivine) has been subtracted to the simulated O K-edge ELNES spectrum of stishovite (see Figure 2 in Winkler et al., 2013 and Figure 4 in Kaneko et al., 1998, respectively) to obtain a simulated differential O K-edge ELNES spectrum of « SiO_4 minus SiO_6 » with the same normalization process. The evolution of experimental differential spectra with the thickness is significant. From Figure 6, four peaks can be noticed, located near the same energies than the simulated differential spectrum ones, that is, 535, 537.5, 539.5, and 543 eV, respectively. The peak situated at 535 eV is negative, and the last peak (at 543 eV) is positive with a small intensity. The two other peaks are positive with medium intensities. Regardless of the studied zones thickness, approximately the same differential ELNES signatures are noted as the simulated ones. This confirms the hypothesis of the occurrence of silicon in octahedral sites in the lamella and hence the identification of Anh-B.

3. Atomic Scale Modeling

To provide further information on the Anh-B structure, calculations based on the density functional theory were performed using the VASP simulation package (Kresse & Hafner, 1993). All results are calculated using generalized gradient approximation (Perdew & Wang, 1992) with pseudopotential (of PAW type) based upon projector-augmented waves (Blöchl, 1994, Kresse & Joubert, 1999). Outmost core radius for Mg, Si, and O atoms are 2, 1.9, and 1.52 au, respectively. Throughout this study, a single cutoff value of 600 eV was used for the plane wave expansion. The first Brillouin zone was sampled using a Monkhorst-Pack grid (Monkhorst & Pack, 1976). For the Anh-B orthorhombic unit cell, using a 6×4×4 mesh leads to convergence of the energy to better than 0.1 meV/atom. To compute the equation of state (EOS; Figure 7) and determine the elastic constants at a given pressure, we first calculate the equilibrium structure of a unit cell by minimizing the Hellman-Feynman forces and stresses. Then, the elastic constants are computed by applying strains (magnitude ±1%) and calculating the resulting stress tensor.
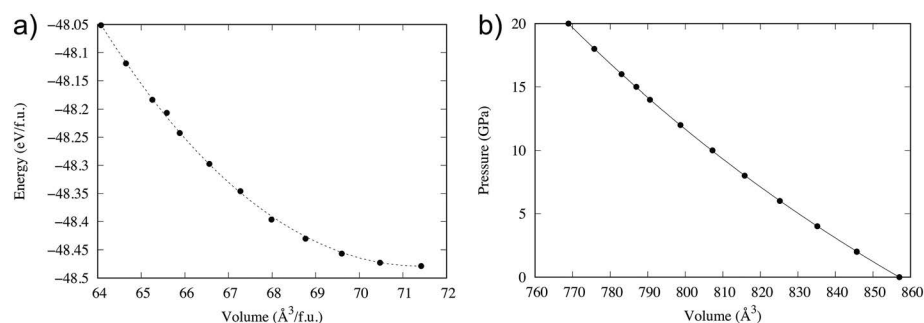
Figure 7. Atomic scale modeling of anhydrous phase B. (a) Energy as a function of the volume. (b) Equation of state, fit function according to the third-order Birch-Murnaghan equation.

At ambient pressure, the lattice parameters for the pure Mg end-member of the Anh-B ($Mg_{14}Si_5O_{24}$ with 86 atoms in the unit cell) are 0.591, 1.429, and 1.014 nm. At 15 GPa, the lattice parameters are 0.574, 1.394, and 0.983 nm. The pressure-volume calculations were fitted to a third-order Birch-Murnaghan EOS to yield B_0=146.86 GPa and B'_0=4.17. The bulk modulus B_0 is in agreement with the experimental one from Crichton et al. (1999): $B_{0, exp}$=151.5 GPa. We note however that its pressure derivative derived from experiments is slightly higher ($B'_{0, exp}$=5.5). Nevertheless, our calculations are somewhat consistent with those reported by Ottonello et al. (2010) using a different density functional method. According to the EOS, the bulk modulus at 15 GPa is thus 209.45 GPa.

According to the computation of the elastic constant tensor at 15 GPa (Table 1), the bulk modulus defined as an average between Voigt and Reuss calculations is 209.21 GPa, self-consistent with the value deduced from the EOS. The shear modulus is 119.7 GPa.

4. Seismic Properties

The elastic constants calculated above can be used to assess the seismic properties of Anh-B. At 0 K and 15 GPa, Anh-B displays moderate seismic anisotropy (Figure 8), which is lower than the intrinsic anisotropy of olivine and wadsleyite (Mainprice, 2007). However, the geometry of anisotropy is similar to that of wadsleyite (Mainprice, 2007). The maximum *P* wave anisotropy is 7%, with the fastest *P* waves propagating parallel to [010] and the slowest, parallel to [001].

S wave polarization anisotropy has a complex pattern. The maximum *S* wave polarization anisotropy (6.1%) is observed for *S* waves propagating obliquely to all three main crystallographic axes, close to [111] directions. These *S* waves are polarized parallel to <uv0> directions. Low *S* wave polarization anisotropy (<2%) is observed for propagation directions along (100) and (010) planes, except parallel to [001] and [100], where intermediate polarization anisotropy values (2.5-3%) and fast polarizations parallel to [100] are observed. Apparent *S* wave polarization isotropy is observed for propagation parallel to [010] or within approximately 25° of [100].

Vs1 velocity patterns show maximum velocities for propagation directions at low angle to <210> directions and minimum velocities for propagation directions parallel to [010] and <201>. When propagating within the (010) plane, Vs1 velocities are rather low and display a 90° periodicity. Low Vs1 propagation anisotropy (<3.5%) is observed within this plane, as well as within the (100) plane. The highest Vs1 propagation

Table 1
Elastic Constants (GPa) and Average Moduli (GPa) of Anh-B Computed at 15 GPa

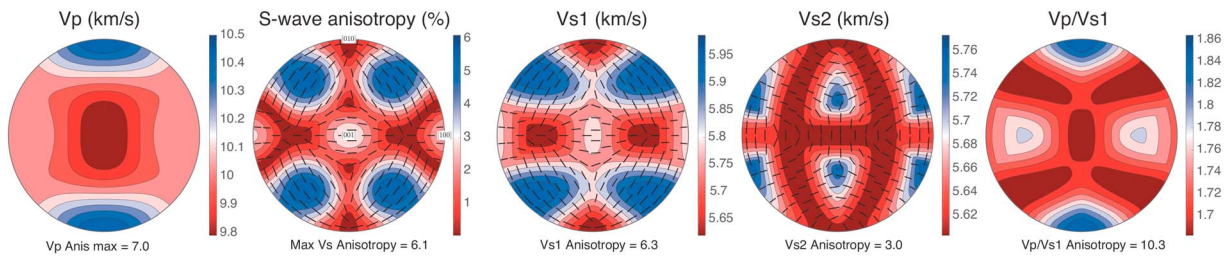| C_{11}	C_{22}	C_{33}	C_{12}	C_{13}	C_{23}	C_{44}	C_{55}	C_{66}
370.7	402.1	349.6	124.5	129.6	127.3	114.5	122.5	115.7
B_V	209.4		B_R	208.9				
G_V	119.9		G_R	119.5				

Note. Pmcb space group.

Figure 8. Seismic properties of anhydrous phase B at 0 K and 15 GPa calculated based on the lattice parameters and elastic constants calculated in this study using the MTEX open-source Matlab toolbox (Mainprice et al., 2011). From left to right: *P* wave propagation anisotropy, *S* wave polarization anisotropy, fast *S* wave (S1) propagation anisotropy, slow *S* wave (S2) propagation anisotropy, and Vp/Vs1 ratio. Lower hemisphere stereographic projections in the crystal reference frame (indicated in the *S* wave polarization anisotropy plot).

anisotropy is observed for propagation within the (001) plane. Vs2 velocities are low for propagation directions parallel to all three main crystallographic axes and minimum for propagation parallel to [010] and [001], as well as at approximately 20-30° to the (100) plane and in the (010) plane at >30° to [100]. High Vs2 are observed for propagation in the (001) plane at approximately 30° to [100] and in the (100) plane at approximately 30° to [001].

Vp/Vs1 ratios are highly anisotropic. The highest ratios (1.86) are observed for propagation directions parallel to [010]. All propagation directions at >20° to [010] sample Vp/Vs1 ratios <1.8.

5. Discussion

This study describes a microstructural characterization with the TEM of a sample of San Carlos olivine partially transformed to wadsleyite at high-pressure (14 GPa) and temperature (1400 °C). At the SEM scale, the transformation into wadsleyite (in the form of irregular domains at grain boundaries or inside grains) was readily observed. However, some lamellae with morphologies clearly distinct from the wadsleyite domains were also present. At the TEM scale, we have used the recently developed (Rauch et al., 2008, 2010) ACOM-TEM technique to identify the phases on FIB sections containing all phases of interest. In this technique, a collection of electron diffraction spot patterns is acquired, while an area of interest of the sample is scanned by the electron beam. The recorded electron diffraction spot patterns are compared with templates calculated for all possible orientations of the phases expected to be present in the area of interest. We have calculated templates corresponding to olivine, wadsleyite, and ringwoodite using crystallographic data from Birle et al. (1968), Horiuchi and Sawamoto (1981), and Hazen et al. (1993), respectively. The olivine matrix and wadsleyite grains resulting from the HP-HT treatment were readily indexed. The lamella identified at the SEM scale was not recognized to be one of those three phases.

5.1. Identification of Anh-B

The observation of the FIB section using diffraction contrast (bright- and dark-fields) yielded additional information. First, the grains indexed as wadsleyite by the ACOM-TEM indeed contain the characteristic stacking faults (Figure 3a) usually found in this mineral. The 320-nm-thick lamella (observed at the SEM) shows no defects. At the TEM, we see that this lamella located at the interface between two olivine grains is not unique in the FIB section. Some much thinner (10-20 nm) lamellae with the same orientation are found in the olivine grain at the bottom of Figure 3. We assume that all those lamellae are constituted of the same phase. This assumption has not been demonstrated but is at least compatible with the chemical analyses performed (see Figure 4). A striking observation is the existence of topotactic relationships between the lamellae and the parent olivine. This is illustrated by Figure 3b, which shows that both the lamella and olivine can be imaged in weak-beam dark-field with very close diffraction vectors (g = 004 for olivine and g = 400 for Anh-B). On this figure, one can see the network of interfacial dislocations, which accommodate the small lattice parameter difference between the two structures in contact. The topotactic relationship between the two structures is along the $(100)_{ol}$ plane of olivine, which corresponds to the $(010)_{Anh-B}$ plane of Anh-B. Indeed, the crystal structures of olivine and Anh-B are very close. The $[100]_{Anh-B}$ direction of Anh-B in *Pmcb* corresponds to $[001]_{ol}$ in olivine. The $[010]_{Anh-B}$ direction of Anh-B corresponds to $[100]_{ol}$ in olivine and represents a superstructure of it. The $[001]_{Anh-B}$ direction of Anh-B corresponds to $[010]_{ol}$ in
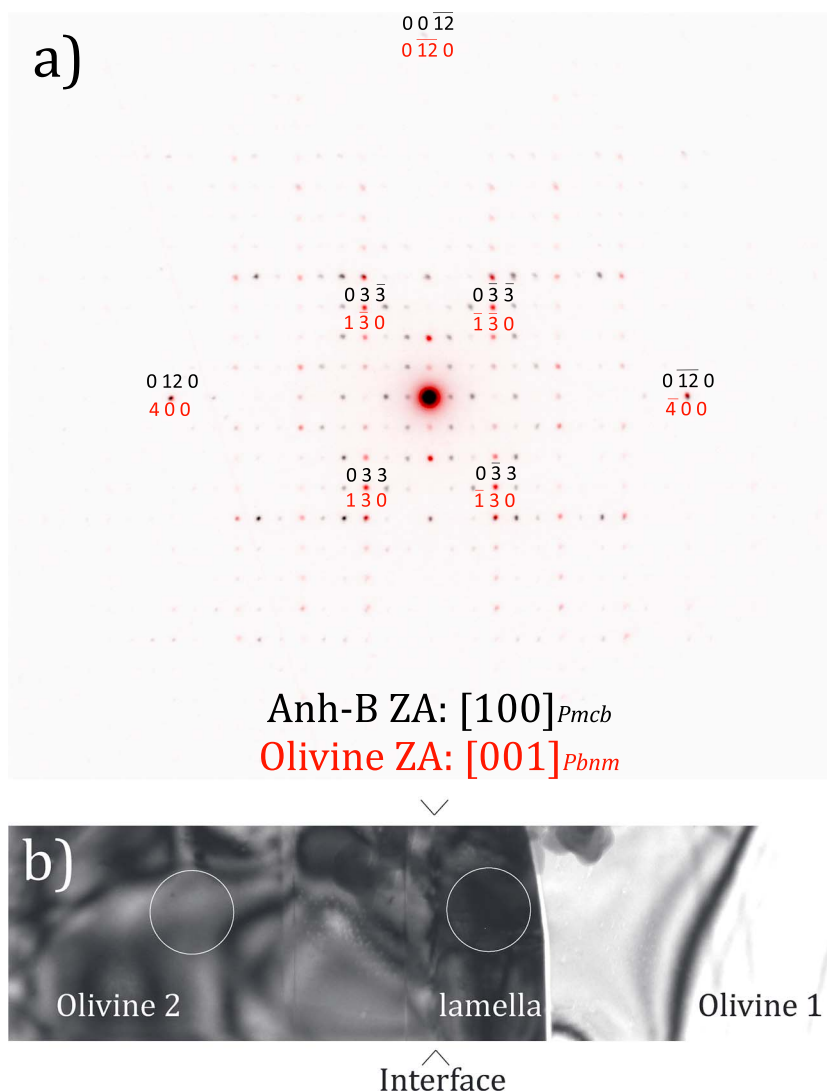
Figure 9. (a) Superimposition of the diffraction patterns acquired on the anhydrous phase B (Anh-B) lamella (colored in black) and in olivine 2, near the lamella (colored in red). The exact locations are shown in (b). A precession angle of 3° has been applied to the electron beam to get quasi-kinematic conditions. A superstructure can be noted between the $[100]_{ol}$ direction of olivine and the $[010]_{Anh-B}$ direction of Anh-B (3×0.48 nm ≈ 1.43 nm); and a correspondence is observed between the $[010]_{ol}$ direction of olivine and the $[001]_{Anh-B}$ direction of Anh-B. (b) Transmission electron microscopy bright-field corresponding to the acquisition of the diffraction patterns of (a). The interface between the lamella and olivine 2 is edge-on and located between the arrows. It corresponds to $(100)_{ol}$ plane in olivine and $(010)_{Anh-B}$ in Anh-B. The circles (250 nm in diameter) represent the position of the selected-area aperture for acquisition of the diffraction patterns of (a).

olivine. These relationships are well illustrated when superimposing diffraction patterns from both phases as shown on Figure 9. Additional examples (from calculated diffraction patterns) are presented in Figure S4.

The determination of crystal structure models is now possible from electron diffraction data (Kolb et al., 2007, 2008; Palatinus, Corrêa, et al., 2015; Palatinus, Petříček, & Correa, 2015; Wan et al., 2013). This allows, as in the present case, to characterize phases with volumes so small that single-crystal X-ray diffraction is precluded. Here some lamellae are large enough for selected area electron diffraction to be performed without sampling the matrix. The analyzed volume is smaller than 0.005 μm³. To get the maximum coverage of the reciprocal space, which is necessary to produce reliable structure model, we use here precession electron diffraction tomography, which combines precession electron diffraction (Vincent & Midgley, 1994) and electron diffraction tomography. For the tomography, we use a tilt range of ± 45° in the microscope.

Combined with the use of precession, this allows a broad coverage of the reciprocal space, which is satisfactory for three-dimensional structure determination. In precession electron diffraction, the electron beam is tilted away from the optical axis of the microscope and precessed on a conical surface with a semi-angle usually between 1 and 3° (here 1.20°). This technique has two advantages: precession electron diffraction patterns are less dynamical and they display a larger number of reflections. Despite that, taking into account dynamical effects is important for the accurate structure refinement (Palatinus, Petříček, & Correa, 2015). The crystal structure model obtained from this data processing is characterized by having part of silicon in sixfold coordination.

Since the discovery of stishovite (Chao et al., 1962; Stishov & Popova, 1961), it is well known that with increasing pressure (between 8 and approximately 30 GPa) most crustal silicates undergo phase transformations to new structures with sixfold coordinated silicon (Finger & Hazen, 1991). In the Earth, this transformation is achieved below 670-km depth. This is however usually not observed in Mg_2SiO_4 since all high-pressure polymorphs known of olivine involve fourfold coordinated silicon. Since this characteristic (silicon in sixfold coordination in the crystal structure model) was critical in the identification of the phase, we decided to carry on an ELNES characterization at the O K-edge, which did confirm the presence of sixfold coordinated silicon. The structure model obtained from the structure refinement, which corresponds to Anh-B, is thus in agreement with all our observations. It also fully explains the chemical composition measured since, starting from an olivine composition, the formation of Anh-B leads to an excess of silica (equation (2)), which was indeed visible on the chemical maps (Figures 4b and 4c). At the pressure considered here, the thin silica layer observed on one side of the lamella is likely stishovite, although we have not checked the crystal structure.

5.2. Stability and Conditions of Formation

The formation of Anh-B was not expected and is a priori surprising since the annealing was carried out in the stability field of wadsleyite (which is indeed observed). To synthesize Anh-B, Ganguly and Frost (2006) started with oxide mixtures, which corresponded to a composition enriched in MgO compared to forsterite. In this system, our conditions (14 GPa, 1400 °C) would indeed favor the formation of Anh-B (see Figure 1 of Ganguly & Frost, 2006, and also the results of calculations from Ottonello et al., 2010, from their Figure 6). This can further be verified by computing the enthalpy change corresponding to the destabilization of Mg_2SiO_4 units into Anh-B and stishovite (St) following the reaction:

$$7.Mg_2SiO_4(Fo, Wa, Ri) \rightarrow Mg_{14}Si_5O_{24}(Anh-B) + 2.SiO_2 (St) \qquad (2)$$
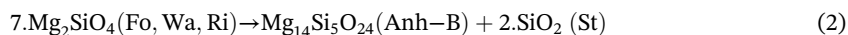
According to the energy computed here for Anh-B (Figure 7) and combining with those computed by Hernández et al. (2015) using the same set of pseudo potentials, we verified that above 14 GPa, the mixture Anh-B + stishovite is indeed a little bit more stable than forsterite but less stable than wadsleyite. Ganguly and Frost (2006) have also calculated the possible reactions (Fo/Wads/Ring) = Anh-B + Stishovite. They show that at 1400 °C, the formation of Anh-B is indeed not expected. To grow Anh-B, Kojitani et al. (2017) and Yuan et al. (2018) started from mixtures having the stoichiometric composition of Anh-B. Alternatively, Anh-B has first been reported by Herzberg and Gasparik (1989) from melting experiments at 16.5 GPa on chondritic material, and in the run product of melting experiments of forsterite at 16.5 GPa, 2380°C (Presnall & Gasparik, 1990). To the best of our knowledge, the only report for direct formation of Anh-B from stoichiometric olivine composition has been done by Hazen et al. (1992) in a Fe-bearing system (Fo80). The unexpected stability of Anh-B was attributed to the presence of Fe.

Most of the thermodynamic approaches (e.g., Ottonello et al., 2010, or the discussion above regarding the reaction enthalpy of equation (2)) do not describe however an important stage, which is nucleation. During solid-state transformation when a product phase nucleates within the parent phase, the energy balance does correspond not only to the volume free energy but also to the interfacial energy. A combination of the two energies constrains the nucleation barrier. In the present case, we see that unlike wadsleyite, which forms irregular domains (inside olivine grains or at grain boundaries) with no preferential orientations with olivine, Anh-B nucleates as thin lamellae. Most of them are inside the grains. We note that the larger one occurs at a grain boundary, which exhibits a specific orientation. This orientation yields a very small interfacial energy, which corresponds to the dislocation network observed on Figure 3b. For that

reason, the energy barrier for nucleation of Anh-B is likely smaller than for wadsleyite. As the phase grows, the contribution of interfacial energy becomes smaller and growth of the thermodynamically stable wadsleyite dominates. Another factor also probably inhibits the growth of Anh-B. It must be remembered that only one side of the lamella can benefit from this low-energy interface. On the other side grows the stishovite layer. We have no hint as to whether the Anh-B/stishovite and stishovite/olivine interfaces have high or low interfacial energies. Also, besides equilibrium thermodynamics considerations, this decomposition into Anh-B and stishovite must slow down as growth proceed since it requires diffusion of O and most importantly of Si across the Anh-B lamella toward the stishovite lamella.

To summarize, we have enough elements to rationalize the observation of Anh-B in our experiments and understand that during a short interval, which corresponds to the nucleation stage, nucleation of Anh-B can compete with the one of wadsleyite. However, one can expect, in agreement with the observed microstructure (see Figure 1), that in the transition zone, growth of wadsleyite rapidly exceeds growth of Anh-B. The situation is different if some MgO-enriched or SiO_2-depleted regions exist. Several studies have suggested the existence of P-T conditions where Anh-B might be stable (Ganguly & Frost, 2006; Ottonello et al., 2010; Yuan et al., 2018). Our study shows that transformation from olivine can be facilitated due to low nucleation energy barriers. Also, one can expect that crystal preferred orientations of Anh-B could be inherited from those of olivine (if they exist).

5.3. Elastic and Seismic Properties, Occurrence in the Mantle, and Detectability

Anh-B might form in places characterized by an enrichment of MgO or a depletion of SiO_2. Yuan et al. (2018) suggest that "MgO-rich compounds might be produced through incongruent melting of both anhydrous and hydrous peridotites" or from the reduction of subducted carbonates. Ganguly and Frost (2006) have proposed that an assemblage Anh-B + stishovite might develop in cold slabs. To evaluate whether the presence of Anh-B can be detected through a seismic signature, we have calculated its elastic and seismic properties. The elastic properties of Anh-B can be compared to those of forsterite calculated at the same pressure, 15 GPa (Durinck et al., 2005). With a bulk modulus 5% larger and a shear modulus 20% larger, Anh-B appears slightly stiffer than forsterite. Anh-B is also more isotropic from the elastic point of view. Taking the orientation relationships between Anh-B and olivine into account, one can compare their elastic constants. In olivine, the three longitudinal moduli are significantly different: C_{22} is 37% softer than C_{11} and C_{33} is 27% softer than C_{11}. In Anh-B, C_{33} (equivalent to C_{22} in olivine) is only 13% softer than C_{22} (equivalent to C_{11} in olivine) and C_{11} (equivalent to C_{33} in olivine) is only 8% softer than C_{22}. For both structures, the off-diagonal moduli (C_{12}, C_{13} and C_{23}) exhibit very similar values. Concerning the shear moduli, in olivine, C_{44} is 10% softer than C_{55} and 15% softer than C_{66}. In Anh-B, the situation is comparable, but with an opposite variation since C_{55} (equivalent to C_{44} in olivine) is 7% stiffer than C_{44} and 6% stiffer than C_{66}. This explains that Anh-B displays only a moderate seismic anisotropy. Moreover, although it is less anisotropic, the seismic anisotropy pattern of the Anh-B crystal is similar to the wadsleyite one (Mainprice, 2007). It seems thus difficult to observe a clear seismic signature of the presence of Anh-B in MgO-rich or SiO_2-depleted regions of the transition zone. If Anh-B forms from olivine in cold slabs, as proposed by Ganguly and Frost (2006), the strongest signal in terms of seismic anisotropy may result from the presence of stishovite, which is one of the most anisotropic phases in the mantle (especially for *S* waves; see Mainprice et al., 2000). The volume fraction of stishovite is however expected to be very small and significant crystal preferred orientations would be necessary for it be detected. As discussed above, they could be inherited from those in olivine.

6. Conclusions

Here we demonstrate that structure refinement can be performed from processing three-dimensional precession electron diffraction data acquired on sample volumes smaller than 0.005 μm^3 of a high-pressure phase. The technique produces a structure model, which is compatible with the chemical composition measured in the TEM by EDS and for which the presence of six-coordinated silicon has been confirmed by EELS analyses.

In this study, we document the formation of Anh-B (and stishovite) in San Carlos olivine at *P*=14 GPa and *T*=1400 °C. At these conditions, the stable phase would be wadsleyite, and indeed, we do see the formation of wadsleyite. In contrast to wadsleyite that occur both on grain-boundaries and inside of grains with little

topotactic relationships to the host (olivine), Anh-B crystals show strong topotactic relationships to parent olivine grains. This suggests that in olivine, Anh-B (and stishovite) can form due to kinetic reasons (lower nucleation energy barrier) as a meta-stable phase.

References

Akaogi, M., Ito, E., & Navrotsky, A. (1989). Olivine-modified spinel-spinel transitions in the system Mg_2SiO_4–Fe_2SiO_4: calorimetric measurements, thermochemical calculation, and geophysical application. *Journal of Geophysical Research*, *94*(B11), 15,671–15,685. https://doi.org/10.1029/JB094iB11p15671

Birle, J. D., Gibbs, G. V., Moore, P. B., & Smith, J. V. (1968). Crystal structures of natural olivines. *American Mineralogist*, *53*, 807–824.

Blöchl, P. E. (1994). Projector augmented-wave method. *Physical Review B*, *50*(24), 17953–17979. https://doi.org/10.1103/PhysRevB.50.17953

Chao, E. C. T., Fahey, J. J., Littler, J., & Milton, D. J. (1962). Stishovite, SiO_2, a very high pressure new mineral from meteor crater, Arizona. *Journal of Geophysical Research*, *67*(1), 419–421. https://doi.org/10.1029/JZ067i001p00419

Cliff, G., & Lorimer, G. (1975). Quantitative analysis of thin specimens. *Journal of Microscopy*, *103*(2), 203–207. https://doi.org/10.1111/j.1365-2818.1975.tb03895.x

Colmont, M., Palatinus, L., Huvé, M., Kabbour, H., Saitzek, S., Djelal, N., & Roussel, P. (2016). On the use of dynamical diffraction theory to refine crystal structure from electron diffraction data: Application to $KLa_5O_5(VO_4)_2$, a material with promising luminescent properties. *Inorganic Chemistry*, *55*(5), 2252–2260. https://doi.org/10.1021/acs.inorgchem.5b02663

Crichton, W. A., Ross, N. L., & Gasparik, T. (1999). Equations of state of magnesium silicates anhydrous B and superhydrous B. *Physics and Chemistry of Minerals*, *26*(7), 570–575. https://doi.org/10.1007/s002690050220

Durinck, J., Legris, A., & Cordier, P. (2005). Pressure sensitivity of olivine slip systems: First-principle calculations. of generalised stacking faults. *Physics and Chemistry of Minerals*, *32*(8-9), 646–654. https://doi.org/10.1007/s00269-005-0041-2

Finger, L., Ko, J., Hazen, R. M., Gasparik, T., Hemley, R. J., Prewitt, C. T., & Weidner, D. J. (1989). Crystal chemistry of phase B and an anhydrous analogue: Implications for water storage in the upper mantle. *Nature*, *341*(6238), 140–142. https://doi.org/10.1038/341140a0

Finger, L. W., & Hazen, R. M. (1991). Crystal chemistry of six-coordinated silicon: A key to understanding the Earth's deep Interior. *Acta Crystallographica*, *B47*, 561–580.

Finger, L. W., Hazen, R. M., & Prewitt, C. T. (1991). Crystal structures of $Mg_{12}Si_4O_{19}(OH)_2$ (phase B) and $Mg_{14}Si_5O_{14}$ (phase AnhB). *American Mineralogist*, *76*, 1–7.

Ganguly, J., & Frost, D. J. (2006). Stability of anhydrous phase B: Experimental studies and implications for phase relations in subducting slab and the X discontinuity in the mantle. *Journal of Geophysical Research*, *111*, B06203. https://doi.org/10.1029/2005JB003910

Garvie, L. A. J. (2010). Can electron energy-loss spectroscopy (EELS) be used to quantify hydrogen in minerals from the O K edge? *American Mineralogist*, *95*(1), 92–97. https://doi.org/10.2138/am.2010.3290

Gasparik, T. (1996). Melting experiments on the enstatite-diopside join at 70-224 kbar, including the melting of diopside. *Contributions to Mineralogy and Petrology*, *124*(2), 139–153. https://doi.org/10.1007/s004100050181

Hazen, R. M., Downs, R. T., & Finger, L. W. (1993). Crystal chemistry of ferromagnesian silicate spinels: Evidence for Mg-Si disorder. *American Mineralogist*, *78*, 1320–1323.

Hazen, R. M., Finger, L. W., & Ko, J. (1992). Crystal chemistry of Fe-bearing anhydrous phase B: Implication for transition zone mineralogy. *American Mineralogist*, *77*, 217–220.

Hernández, E. R., Brodholt, J., & Alfè, D. (2015). Structural, vibrational and thermodynamic properties of Mg_2SiO_4 and $MgSiO_3$ minerals from first-principles simulations. *Physics of the Earth and Planetary Interiors*, *240*, 1–24. https://doi.org/10.1016/j.pepi.2014.10.009

Herzberg, C., & Gasparik, T. (1989). Melting experiments on chondrite at high pressures: stability of anhydrous Phase B. *Eos*, *70*, 484.

Hirose, K. (2002). Phase transitions in pyrolitic mantle around 670-km depth: Implications for upwelling of plumes from the lower mantle. *Journal of Geophysical Research*, *107*(B4), 2078. https://doi.org/10.1029/2001JB000597

Horiuchi, H., & Sawamoto, H. (1981). Beta-Mg_2SiO_4: Single-crystal X-ray diffraction study. *American Mineralogist*, *66*, 568–575.

Irifune, T. (1987). An experimental investigation of the pyroxene-garnet transformation in a pyrolite composition and its bearing on the constitution of the mantle. *Physics of the Earth and Planetary Interiors*, *45*(4), 324–336. https://doi.org/10.1016/0031-9201(87)90040-9

Kaneko, K., Tanaka, I., & Yoshiya, M. (1998). Six-fold coordinated silicon at grain boundaries in sintered α-Al_2O_3. *Applied Physics Letters*, *72*(2), 191–193. https://doi.org/10.1063/1.120681

Katsura, T., & Ito, E. (1989). The system Mg_2SiO_4–Fe_2SiO_4 at high pressures and temperatures: precise determination of stabilities of olivine, modified spinel and spinel. *Journal of Geophysical Research*, *94*(B11), 15,663–15,670. https://doi.org/10.1029/JB094iB11p15663

Katsura, T., Yamada, H., Nishikawa, O., Song, M., Kubo, A., Shinmei, T., et al. (2004). Olivine-wadsleyite transition in the system (Mg, Fe)$_2SiO_4$. *Journal of Geophysical Research*, *109*, B02209. https://doi.org/10.1029/2003JB002438

Kresse, G., & Joubert, D. (1999). From ultrasoft pseudopotentials to the projector augmented-wave method. *Physical Review B*, *59*(3), 1758–1775. https://doi.org/10.1103/physrevb.59.1758

Kojitani, H., Terata, S., Ohsawa, M., Mori, D., Inaguma, Y., & Akaogi, M. (2017). Experimental and thermodynamic investigations on the stability of $Mg_{14}Si_5O_{24}$ anhydrous phase B with relevance to Mg2SiO4 forsterite, wadsleyite, and ringwoodite. *American Mineralogist*, *102*(10), 2032–2044. https://doi.org/10.2138/am-2017-6115

Kolb, U., Gorelik, T., Kuebel, C., Otten, M. T., & Hubert, D. (2007). Towards automated diffraction tomography: Part I—Data acquisition. *Ultramicroscopy*, *107*(6-7), 507–513. https://doi.org/10.1016/j.ultramic.2006.10.007

Kolb, U., Gorelik, T., & Otten, M. T. (2008). Towards automated diffraction tomography. Part II—Cell parameter determination. *Ultramicroscopy*, *108*(8), 763–772. https://doi.org/10.1016/j.ultramic.2007.12.002

Kresse, G., & Hafner, J. (1993). Ab initio molecular dynamics for liquid metals. *Physical Review B*, *47*(1), 558–561. https://doi.org/10.1103/PhysRevB.47.558

Mainprice, D. (2007). Seismic anisotropy of the deep Earth from a mineral and rock physics perspective. *Treatise of Geophysics*, *2*, 437–491. https://doi.org/10.1016/B978-044452748-6.00045-6

Mainprice, D., Barruol, G., & Ben Ismaïl, W. (2000). The seismic anisotropy of the Earth's mantle: From single crystal to polycrystal. In S.-I. Karato, A. Forte, R. Liebermann, G. Masters, & L. Sixrude (Eds.), *Earth's deep interior: Mineral physics tomography from atomic scale to the global scale*, Geophys. Monogr, (Vol. 117, pp. 237–264). Washington, DC: American Geophysical Union.

Mainprice, D., Hielscher, R., & Schaeben, H. (2011). Calculating anisotropic physical properties from texture data using the MTEX open source package in Prior, D.J., Rutter, E.H., Tatham, D. J. (eds) Deformation mechanisms, rheology and tectonics: Microstructures, mechanics and anisotropy. *Geological Society, London, Special Publications*, *360*(1), 175–192. https://doi.org/10.1144/SP360.10

Mkhoyan, K. A., Silcox, J., Ellison, A., Ast, D., & Dieckmann, R. (2006). Full recovery of electron damage in glass at ambient temperatures. *Physical Review Letters*, *96*(20), 205506. https://doi.org/10.1103/PhysRevLett.96.205506

Monkhorst, H. J., & Pack, J. D. (1976). Special points for Brillouin-zone integrations. *Physical Review B*, *13*(12), 5188–5192. https://doi.org/10.1103/PhysRevB.13.5188

Ottonello, G., Civalleri, B., Ganguly, J., Perger, W. F., Belmonte, D., & Vetuschi Zuccolini, M. (2010). Thermo-chemical and thermo-physical properties of the high-pressure phase anhydrous B ($Mg_{14}Si_5O_{24}$): An ab-initio all-electron investigation. *American Mineralogist*, *95*(4), 563–573. https://doi.org/10.2138/am.2010.3368

Palatinus, L. (2011), PETS—Program for analysis of electron diffraction data. Institute of Physics, Prague, Czech Republic.

Palatinus, L., Brázda, P., Boullay, P., Perez, O., Klementová, M., Petit, S., et al. (2017). Hydrogen positions in single nanocrystals revealed by electron diffraction. *Science*, *355*(6321), 166–169. https://doi.org/10.1126/science.aak9652

Palatinus, L., & Chapuis, G. (2007). SUPERFLIP—A computer program for the solution of crystal structures by charge flipping in arbitrary dimensions. *Journal of Applied Crystallography*, *40*(4), 786–790. https://doi.org/10.1107/S0021889807029238

Palatinus, L., Corrêa, C. A., Steciuk, G., Jacob, D., Roussel, P., Boullay, P., et al. (2015). Structure refinement using precession electron diffraction tomography and dynamical diffraction: tests on experimental data. *Acta Crystallographica Section B*, *71*(6), 740–751. https://doi.org/10.1107/S2052520615017023

Palatinus, L., Petříček, V., & Correa, C. A. (2015). Structure refinement using precession electron diffraction tomography and dynamical diffraction: theory and implementation. *Acta Crystallogr. Sect. A*, *71*(2), 235–244. https://doi.org/10.1107/S2053273315001266

Perdew, J. P., & Wang, Y. (1992). Accurate and simple analytic representation of the electron-gas correlation energy. *Physical Review B*, *42*, 13,244.

Presnall, D. C., & Gasparik, T. (1990). Melting of enstatite ($MgSiO_3$) from 10 to 16.5 GPa and the forsterite (Mg_2SiO_4)–majorite ($MgSiO_3$) eutectic at 16.5 GPa: Implications for the origin of the mantle. *Journal of Geophysical Research*, *95*(B10), 15,771–15,777. https://doi.org/10.1029/JB095iB10p15771

Rauch, E. F., Portillo, J., Nicolopoulos, S., Bultreys, D., Rouvimov, S., & Moeck, P. (2010). Automated nanocrystal orientation and phase mapping in the transmission electron microscope on the basis of precession electron diffraction. *Zeitschrift für Kristallographie International journal for structural, physical, and chemical aspects of crystalline materials*, *225*(2-3), 103–109. https://doi.org/10.1524/zkri.2010.1205

Rauch, E. F., Véron, M., Portillo, J., Bultreys, D., Maniette, Y., & Nicolopoulos, S. (2008). Automatic crystal orientation and phase mapping in TEM by precession diffraction. *Microscopy and Analysis*, *93*, S5–S8.

Ringwood, A. E. (1991). Phase transformations and their bearings on the constitution and dynamics of the mantle. *Geochemica and Cosmochemica Acta*, *55*(8), 2083–2110. https://doi.org/10.1016/0016-7037(91)90090-R

Rondeau, B., Boulet, C., Corre, M., Mollé, V., Devouard, B., Jacob, D., et al. (2019). Lasnierite, $(Ca,Sr)(Mg,Fe)_2Al(PO_4)_3$, a new phosphate accompanying lazulite from Mt. Ibity, Madagascar: An example of structural characterization from dynamical refinement of precession electron diffraction data on submicrometre sample. *European Journal of Mineralogy*, *31*(2), 379–388. https://doi.org/10.1127/ejm/2019/0031-2817

Roussel, P., Palatinus, L., Belva, F., Daviero-Minaud, S., Mentre, O., & Huve, M. (2014). $Sr_4Ru_6ClO_{18}$, a new $Ru^{4+/5+}$ oxy-chloride, solved by precession electron diffraction: Electric and magnetic behavior. *Journal of Solid State Chemistry*, *212*, 99–106. https://doi.org/10.1016/j.jssc.2014.01.012

Sharp, T., Wu, Z., Seifert, F., Poe, B., & Doerr, M. (1996). & Paris, E. (1996), Distinction between six- and fourfold coordinated silicon in SiO_2 polymorphs via electron loss near edge structure (ELNES) spectroscopy. *Physics and Chemistry of Minerals*, *23*(1), 17–24. https://doi.org/10.1007/BF00202989

Stishov, S. M., & Popova, S. V. (1961). New dense polymorphic modification of silica. *Geokhimiya*, *10*, 837–839. (in Russian)

Tanuma, S., Powell, C. J., & Penn, D. R. (1993). Calculations of electron inelastic mean free paths (IMFPs)IV. Evaluation of calculated IMFPs and of the predictive IMFP formula TPP-2 for electron energies between 50 and 2000 eV. *Surface and Interface Analysis*, *20*(1), 77–89. https://doi.org/10.1002/sia.740200112

Van Cappellen, E., & Doukhan, J. C. (1994). Quantitative transmission X-ray microanalysis of ionic compounds. *Ultramicroscopy*, *53*(4), 343–349. https://doi.org/10.1016/0304-3991(94)90047-7

Vincent, R., & Midgley, P. A. (1994). Double conical beam-rocking system for measurement of integrated electron diffraction intensities. *Ultramicroscopy*, *53*(3), 271–282. https://doi.org/10.1016/0304-3991(94)90039-6

Wan, W., Sun, J., Su, J., Hovmöller, S., & Zou, X. (2013). Three-dimensional rotation electron diffraction: software RED for automated data collection and data processing. *Journal of Applied Crystallography*, *46*(6), 1863–1873. https://doi.org/10.1107/S0021889813027714

Winkler, B., Avalos-Borja, M., Milman, V., Perlov, A., Pickard, C. J., & Yates, J. R. (2013). Oxygen K-edge electron energy loss spectra of hydrous and anhydrous compounds. *Journal of Physics: Condensed Matter*, *25*(48), 485401. https://doi.org/10.1088/0953-8984/25/48/485401

Yuan, L., Ohtani, E., Shibazaki, Y., Ozawa, S., Jin, Z., Suzuki, A., & Frost, D. J. (2018). The stability of anhydrous phase B, $Mg_{14}Si_5O_{24}$, at mantle transition zone conditions. *Physics and Chemistry of Minerals*, *45*(6), 523–531. https://doi.org/10.1007/s00269-017-0939-5